RESEARCH ARTICLE | DECEMBER 03 2025

Nonvolatile bidirectional photoresponse in a fully CMOS-compatible FeFET for in-sensor computing

Yuyan Fan ; Wei Li; Jianquan Liu ; Danyang Chen ; Xinrui Ma ; Tianning Cui ; Zhiyu Lin ; Mengwei Si ; Jingquan Liu ; Gang Liu ; Bobo Tian ; Xiuyan Li

Appl. Phys. Lett. 127, 223303 (2025)
https://doi.org/10.1063/5.0299857

Applied Physics Letters ARTICLE pubs.aip.org/aip/apl

Nonvolatile bidirectional photoresponse in a fully CMOS-compatible FeFET for in-sensor computing

Cite as: Appl. Phys. Lett. **127**, 223303 (2025); doi: 10.1063/5.0299857
Submitted: 29 August 2025 · Accepted: 15 November 2025 ·
Published Online: 3 December 2025

Yuyan Fan,[1,2] Wei Li,[3] Jianquan Liu,[3] Danyang Chen,[1,2] Xinrui Ma,[1,2] Tianning Cui,[1,2] Zhiyu Lin,[2] Mengwei Si,[1] Jingquan Liu,[1] Gang Liu,[4,a)] Bobo Tian,[3,a)] and Xiuyan Li[1,a)]

AFFILIATIONS

[1]National Key Laboratory of Advanced Micro and Nano Manufacture Technology, Shanghai Jiao Tong University, Shanghai 200240, People's Republic of China
[2]School of Integrated Circuits (School of Information Science and Electronic Engineering), Shanghai Jiao Tong University, Shanghai 200240, People's Republic of China
[3]Key Laboratory of Polar Materials and Devices, Ministry of Education, East China Normal University, Shanghai 200241, People's Republic of China
[4]School of Materials, Sun Yat-Sen University, Shenzhen, Guangdong 518107, People's Republic of China

[a)]**Authors to whom correspondence should be addressed:** liugang82@mail.sysu.edu.cn; bbtian@ee.ecnu.edu.cn; and xiuyanli@sjtu.edu.cn

ABSTRACT

While bipolar phototransistors show promise for in-sensor computing, their incompatibility with standard complementary metal–oxide–semiconductor (CMOS) technology has hindered practical integration. In this work, we demonstrate nonvolatile bidirectional photoresponse using a fully CMOS-compatible metal–ferroelectric–metal–insulator–semiconductor ferroelectric field effect transistor with $Hf_{0.5}Zr_{0.5}O_2$ and IGZO materials. The key lies in a floating gate-based ferroelectric-tunable band alignment mechanism, achieving nonvolatile bipolar photoconductive states while reducing write power by two orders of magnitude. Furthermore, high-performance image processing tasks, including image sharpening, edge detection, and motion detection, are implemented using the device. This work presents a promising approach to CMOS-compatible hardware design for future in-sensor computing systems.

The rapid development of the Internet of Things (IoT) has driven an urgent demand for efficient processing of vast visual information. While advanced image sensors are capable of real-time image detection, data transmission between different units causes severe latency and efficiency issues.[1–5] To address this, in-sensor computing has been proposed, which integrates photosensing, memory, and computing functions into a single hardware platform.[1,6,7]

In recent years, emerging devices like resistive switching memories,[8] phase-change memories,[9] atom switch memories,[10] and phototransistors[11,12] have been proposed as potential devices for in-sensor computing. Among them, phototransistors have attracted increasing attention due to their unique advantages of nonvolatile storage, precise gate voltage (V_G) control, low power consumption, and high integration capability,[13–16] and have been widely used in advanced sensing systems. Conventional phototransistors predominantly exhibit only positive photoresponse driven by the generation and dissociation of photo-excited carriers under light.[17–19] In contrast, negative photoresponse, which refers to a decrease in channel conductivity under illumination, is less common and typically occurs under specific conditions of temperature,[20] pressure,[21] atmosphere,[22] or operating voltage.[6,23,24] This special photoresponse exhibits distinct advantages over the positive one, including reduced energy loss and enhanced efficiency,[6] significantly expanding the functionality of traditional photodetectors and enabling advanced applications such as low-power photodetectors,[25] optical logic gates,[26] neuromorphic devices,[27] and multifunctional nonvolatile memories.[28]

Furthermore, by incorporating both positive and negative photoresponses into a single transistor, effective pixel matching with diverse convolution kernels can be achieved at the sensor level, enabling hardware-based convolutional operations.[6,29] This approach not only boosts recognition accuracy and computational efficiency but also streamlines hardware design and further reduces energy consumption.[3,6,23,30] It broadens the applications of phototransistors to optical and electrical dual-control[31] or all-optical control logic devices,[26]

enabling efficient image processing in more complex environments with minimized energy consumption and maximized operational speed.[6,32] For instance, in event camera applications, the cancelation of positive and negative photoresponses in a single phototransistor can highlight moving objects, effectively filtering out static background information and improving recognition efficiency.[3]

Recent studies have investigated bidirectional photoresponse in various material systems. For example, Wang *et al.* demonstrated this phenomenon in a graphene/organic semiconductor heterojunction phototransistor in 2018,[33] and Miao *et al.* and Han *et al.* reported similar photosensing behaviors in ReS_2/h-BN/MoS_2[34] and MoS_2/h-BN/Gr[17] in 2018 and 2022, respectively. However, these materials predominantly rely on low-dimensional (0D-2D),[21,23,24,32,35–37] organic,[38,39] or perovskite-based photosensitive materials,[40–42] which face significant challenges in scalability, environmental stability, and complementary metal–oxide–semiconductor (CMOS) compatibility. In contrast, oxide materials like InO and InGaZnO (IGZO) demonstrate superior scalability, stability, and straightforward integration into existing semiconductor workflows, making them promising candidates.[43,44] Although limited works have explored bidirectional photoresponse in oxide-based systems, organic components are still inevitably introduced.[45–47] Thus, developing a fully CMOS-compatible phototransistor with bidirectional photoresponse remains a significant challenge.

In this work, we employ a fully CMOS-compatible metal–ferroelectric–metal–insulator–semiconductor (MFMIS) ferroelectric field effect transistor (FeFET) with ferroelectric (FE) $Hf_{0.5}Zr_{0.5}O_2$ (HZO) material and IGZO channel to enable bidirectional photoresponse. Both positive and negative photoconductive states are achieved in the device through an FE-tunable band alignment, which facilitates the tunneling of photo-generated holes or electrons from IGZO to the floating gate (FG) under illumination. Benefiting from the nonvolatile polarization of the FE layer, not only are the photoconductive states memorized but the write power consumption is also reduced by two orders of magnitude. Furthermore, high-performance image processing tasks, including image sharpening, edge detection, and motion detection, are implemented using the device. This work presents a promising approach to CMOS-compatible hardware design for future intelligent in-sensor computing.

The MFMIS FeFET was fabricated following a fully CMOS-compatible process, as shown in Fig. 1(a). The device structure is schematically shown in Fig. 1(b), and the optical microscope image from the top of the device is shown in Fig. 1(c). 30 nm TiN was first deposited by sputtering on SiO_2/Si and patterned as the bottom gate (BG)/floating gate (FG), followed by 10 nm HZO by atomic layer deposition (ALD) at 250 °C. Another 30 nm TiN top gate (TG) was then sputtered and patterned, with subsequent 450 °C rapid thermal annealing (RTA) in N_2 for 30 s to crystallize the HZO. Then, a 40 nm IGZO channel was sputtered and etched, followed by 40 nm Ni source/drain (S/D) evaporation and 250 °C RTA (5 min) for Ohmic contacts. All electrical measurements were conducted using a Keithley 4200A SCS Semiconductor Analyzer. Light pulses were controlled by a VB-8012 VisualBench signal generator, allowing for power adjustment via a voltage source.

As we know, the MFMIS FeFET can be modeled as a series connection of a metal–ferroelectric–metal (MFM) capacitor (C_{FE}) and a metal–insulator–semiconductor (MIS) capacitor (C_{IL}),[48] as shown in Fig. 1(d). A key parameter, the area ratio (AR), is defined as the ratio

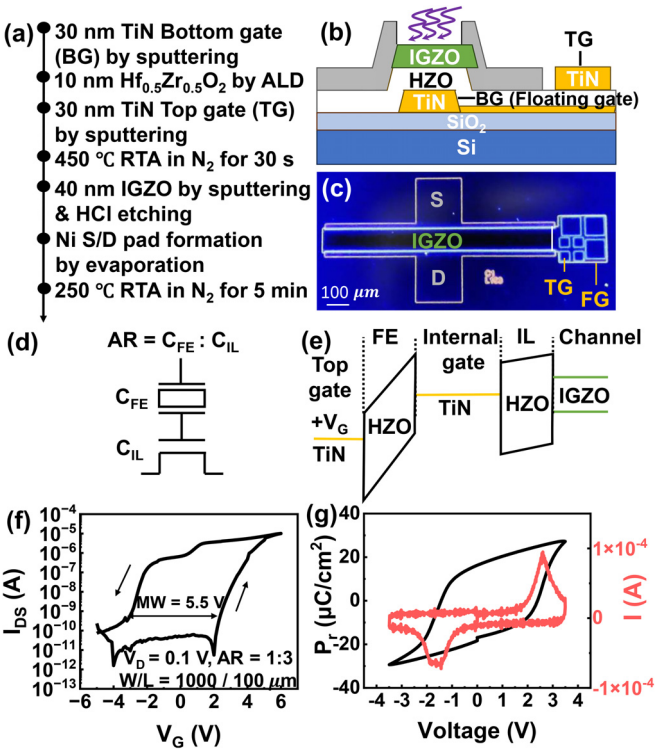

FIG. 1. (a) Device fabrication process; (b) schematic illustration, and (c) optical microscope image of the MFMIS FeFET. (d) Equivalent circuit structure and (e) band diagram illustrating the operation principle of the MFMIS FeFET. (f) Transfer characteristics of the device, demonstrating a large memory window of 5.5 V and an I_{on}/I_{off} ratio of 10^6 at an area ratio (AR) of 1:3. (g) Hysteresis and switching current curves of the gate-integrated MFM capacitor within the MFMIS structure.

of the areas of these two capacitors. The operation mechanism of the device is shown in Fig. 1(e) from the perspective of an energy band diagram. When V_G is applied at the top gate (TG), the voltage is distributed across the FE and insulator layers (IL), and the actual voltage drop across the FE layer determines the memory window (MW).[48–51] In this way, a large MW of 5.5 V is obtained through a low AR of 1:3, with a considerable photosensing area (W/L = 1000/100 μm), as shown in Fig. 1(f). The on/off ratio (I_{on}/I_{off}) also reaches a high value of 10^6. In addition, the ferroelectricity of the gate-integrated MFM capacitor is characterized in Fig. 1(g), and $2P_r$ of ~40 μ C/cm^2 is demonstrated. The GIXRD pattern of HZO is shown in Fig. S1 (supplementary material).

Then, the optoelectronic characteristics of the device under 405 nm light illumination were investigated. Figures 2(a) and 2(b) illustrate the variation of I_{DS} in response to a sequence of light pulses at different V_G, while maintaining a constant light intensity of 1.35 W/cm^2. More specifically, in Fig. 2(a), V_G ranging from 1.5 to 3 V was applied to the TG of the device during the test. Upon illumination, a sharp increase in current is observed, which saturates under light exposure and then rapidly decreases when light is turned off. This behavior demonstrates a typical positive photoresponse of the device. Notably, the condition changes dramatically at a higher $V_G \geq 4$ V, as shown in Fig. 2(b). In this case, a significant decrease in current is

observed during the illumination periods, followed by a gradual recovery of current in the dark. This contrasting behavior highlights the negative photoresponse of the device. The relatively slower decrease and recovery of the current suggest a different physics from the conventional positive photoresponse, which exhibits rapid switching under light. These results demonstrate that the HZO-based MFMIS structure of FeFET exhibits both positive and negative photoresponses under the modulation of V_G. Additionally, a small upward/downward current peak is detected at the instant the light is turned on/off. Given the rapid response speed, these peaks are likely attributed to the generation and recombination of photo-excited carriers in the IGZO layer. Locally magnified close-ups distinguishing the fast peak from the slow tunneling one were shown in Fig. S2 (supplementary material). This observation indicates a potential competition between positive and negative photoresponses within the device, where a higher V_G promotes the dominance of the negative photoresponse over the positive one.

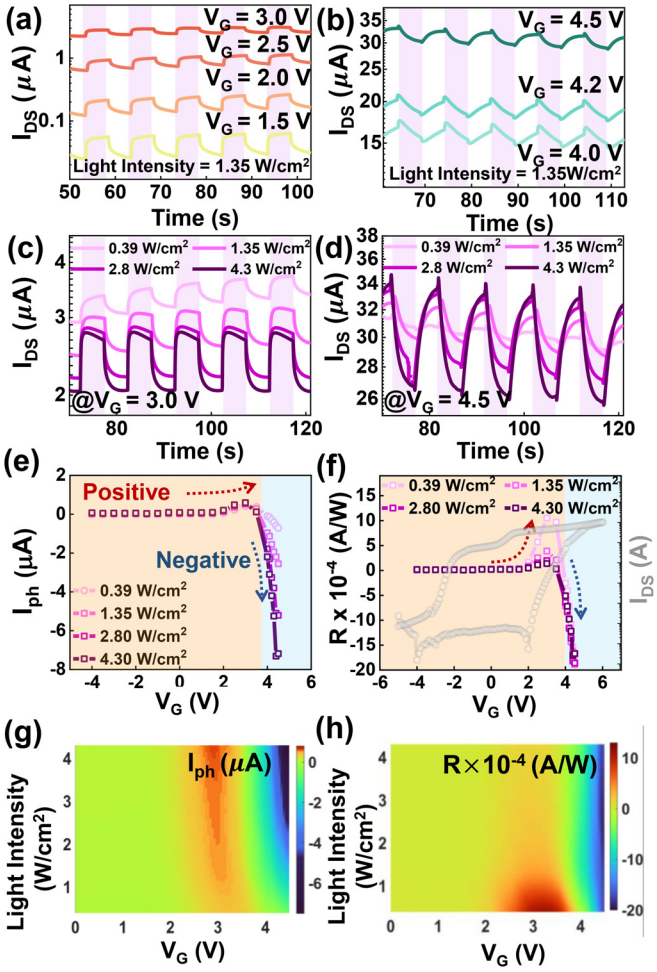

FIG. 2. Gate-tunable bidirectional photoresponse of the device at $V_D = 1$ V under 405 nm illumination. (a) Positive and (b) negative photoresponses under varying V_G. (c) Positive and (d) negative photoresponses at a fixed V_G under different light intensities. (e) Extracted I_{ph} and (f) R as a function of V_G under different light intensities. (g) Mapping of I_{ph} and (h) R with varying V_G and light intensities.

Moreover, the photoresponse under various light intensities was also investigated, as illustrated in Figs. 2(c) and 2(d). The spot size of the light source relative to the single demo device is schematically illustrated in Fig. S3 (supplementary material). In both cases, stronger photoresponses are observed as the light intensity increases. To gain deeper insights into how the photoresponse is influenced by V_G, the photocurrent (I_{ph}) and photoresponsivity (R) under different illumination conditions were extracted as a function of V_G, as shown in Figs. 2(e) and 2(f), respectively. When $V_G < 2$ V (approximately the threshold voltage (V_{th})), no significant change is observed for either I_{ph} or R. Beyond that, both I_{ph} and R increase and reach a maximum around $V_G \sim 3$ V, and then decrease rapidly for $V_G > 3$ V. Notably, a transition from positive to negative photoresponse occurs at $V_G \sim 4$ V. These results clearly demonstrate a significant gate-tuning effect on the photoresponse. More intuitively, mappings of the change in I_{ph} and R with respect to V_G and light intensity are presented in Figs. 2(g) and 2(h), respectively. The absolute value of I_{ph} ($|I_{ph}|$) increases while R decreases with higher light intensities. Importantly, negative I_{ph} and R, corresponding to the negative photoresponse, only appear when V_G exceeds a critical high value around 4 V. The gate-tunable bipolar photoresponse is also investigated by I_{DS}–V_{DS} measurements, under both 405 and 450 nm light, as shown in Fig. S4 (supplementary material). These findings collectively highlight the capability of the device to exhibit gate-modulated bipolar photoresponse behavior.

The above-mentioned measurements were performed with a persistent V_G at the TG, which, however, may lead to power consumption issues. Considering that ferroelectric polarization has been widely applied in nonvolatile memories to reduce energy consumption,[28,52] here, an alternative strategy was tried. First, a negative V_G pulse (−4.5 V, 2 s) was applied at the TG to preset the polarization of the FE layer in the upward direction from FG to TG and then removed before light illumination. As a result, progressive positive photoconductive states were achieved and memorized with a series of light pulses, as shown in Fig. 3(a), under different light intensities. During each optical

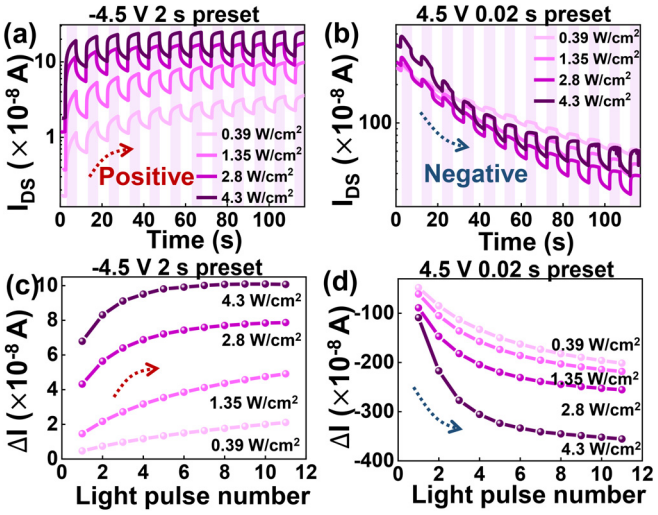

FIG. 3. Nonvolatile (a) positive and (b) negative photoresponses under varying light intensities with an initial preset V_G pulse. (c) and (d) Extracted changes in I_{DS} (ΔI_{DS}) as a function of the number of light pulses.

TABLE I. Comparative analysis of phototransistors exhibiting bidirectional photoresponses, highlighting key parameters: channel material, gate structure, MW, I_{on}/I_{off} ratio, photosensing wavelength, nonvolatility, and CMOS compatibility.

	Ref. 11	Ref. 29	Ref. 53	Ref. 54	This work
Channel	Bilayer MoS_2	$MAPbI_3/Bi_2O_2Se$	Black phosphorus	InO	IGZO
Gate	Al_2O_3	HfO_2	SiO_2	Side-gate ion-gel	TiN/HZO/TiN
MW	2.41 V	⋯	15 V	∼1.5 V	5.5 V
I_{on}/I_{off}	10^9	10^6	4	10^5	10^6
Photosensing wavelength	660 nm	400 nm, 500 nm, 700 nm	White light	520 nm	405 nm, 450 nm
Nonvolatility	Yes	No	Yes	Yes	Yes
CMOS compatibility	No	No	No	No	Yes

operation period, the current rises under illumination, although a decrease in current occurs during the dark intervals, it does not revert the photoconductivity to its initial pre-illumination value. Consequently, the photoconductive states are effectively memorized. Similarly, after applying a positive V_G pulse (4.5 V, 0.02 s), the polarization of the FE layer was preset in the downward direction from TG to FG; in this case, progressive negative photoconductive states are achieved, as shown in Fig. 3(b). The retention of nonvolatile negative photoresponse, exceeding 100 s after one illumination period, was presented in Fig. S5 (supplementary material). During the illumination periods, a sustained decrease in current is observed. The overall trend of current with light pulses reflects a reduction in photoconductivity, indicating a dominant nonvolatile negative photoresponse. Therefore, taking advantage of the nonvolatility of the FE layer, both positive and negative photoconductivity are achieved and memorized in the device without persistent V_G. The change in I_{DS} (ΔI_{DS}) with the number of light pulses in both cases was also extracted, as shown in Figs. 3(c) and 3(d), respectively, which will serve as optical weights in image processing tasks discussed later. In fact, a lower positive V_G could also induce a negative photoresponse, like the case in Fig. 3(b), but the pulse duration should be longer to ensure sufficient polarization switching, as shown in Fig. S6 (supplementary material). Compared with operations that require persistent V_G, benefiting from the nonvolatile polarization of the FE layer, not only is nonvolatile bipolar photoresponse achieved but also the power consumption for each optical operation has been evaluated to be decreased by two orders of magnitude (from 8.2×10^{-9} to 3.2×10^{-11} J). The detailed calculation method is presented in the supplementary material. Compared to other phototransistors that exhibit bipolar photoresponse, our device shows excellent CMOS compatibility with nonvolatile photosensing behaviors,[11,29,53,54] as shown in Table I, offering a promising route to high-performance sensing, computing, and memory integration.

Next, we understand the physical origin of the bidirectional photoresponse of the device. To address the effect of FG in our device, we investigated the optoelectronic behaviors in different structures while keeping the materials unchanged. A stepwise V_G [see the inset of Fig. 4(a)] was exerted on the FG instead of the TG to examine the continuous change of I_{ph} with V_G in an MIS configuration. V_{DS} was set as 1 V, and light intensity was set as 4.3 W/cm^2 to ensure an obvious variation in current. Interestingly, in this MIS case, no negative I_{ph} is observed regardless of V_G, as shown in Fig. 4(a), indicating that the key to the bipolar photoresponse lies in the FG structure of the device. The same measurement condition was also applied to the MFMIS

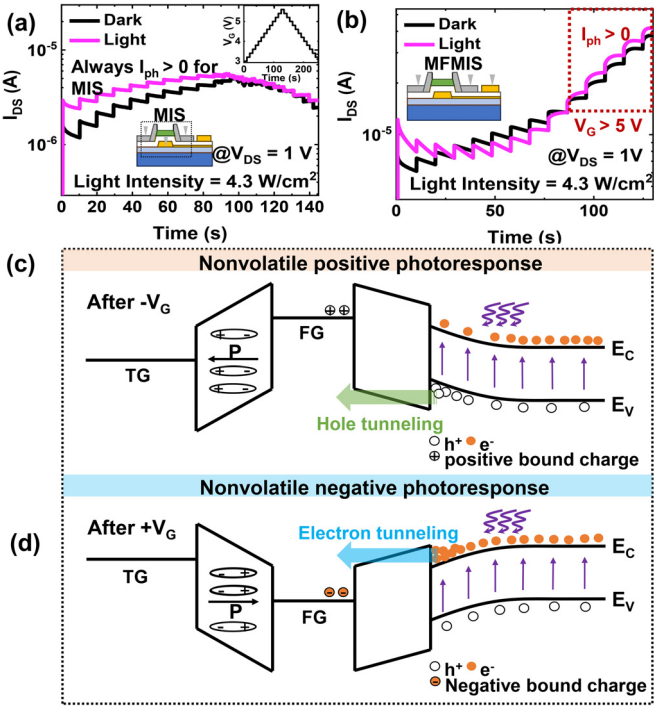

FIG. 4. (a) Temporal evolution of I_{DS} under stepwise V_G in MIS and (b) MFMIS configurations. The inset in (a) illustrates the stepwise V_G scheme applied to the device. Band diagram illustrations of the nonvolatile (c) positive photoresponse and (d) negative photoresponse.

structure. Notably, as shown in Fig. 4(b), although a negative I_{ph} is observed when V_G exceeds a critical value, consistent with what we discussed earlier, a too-high V_G would revert the negative I_{ph} back to positive. This is likely attributed to the breakdown of the FE layer under a rather high voltage, further evidence is shown in Fig. S7 (supplementary material). This phenomenon is common and repeatable in various single demo MFMIS devices with different AR values (see Fig. S8 in the supplementary material). Moreover, different from the reported van der Waals (vdW) heterostructure-based FG structures,[41] in this work, we additionally induce ferroelectricity, which may play a distinct role. Therefore, a device with unannealed HZO, which lacks ferroelectricity, was also investigated. In this metal–insulator–metal–insulator–

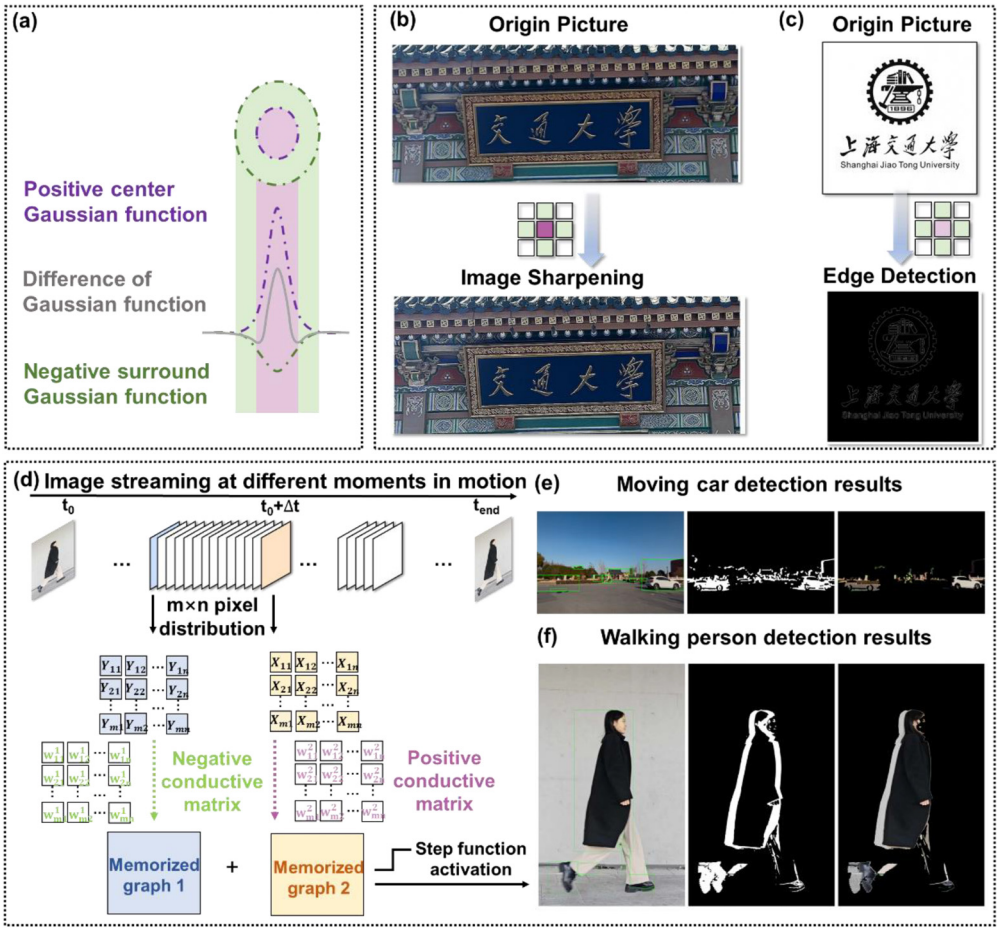

FIG. 5. (a) Schematic representation of receptive fields along with the corresponding difference-of-Gaussians (DoG) curves. (b) Image sharpening and (c) edge detection results. Illustration of motion detection using the simulated arrays: (d) motion image pixels (m × n) at a specific frame difference time are multiplied by the m × n positive and negative conductance matrix of the proposed hardware, with the summed output enabling motion object detection. Processed images demonstrating motion detection for (e) a moving car and (f) a walking person.

semiconductor (MIMIS) structure, although a negative photoresponse also emerges under high V_G (see Fig. S9 in the supplementary material), a persistent V_G is required to maintain the photoconductivity due to the absence of ferroelectric polarization.

Based on the above-mentioned considerations, the nonvolatile bipolar photoresponse can be understood well by a ferroelectric-tunable band alignment mechanism. Specifically, as shown in Fig. 4(c), after a sufficient negative V_G pulse, the polarization is preset upward from FG to TG, causing the energy band of the FE layer to exhibit a downward slope from FG to TG. This tilts the energy band of the insulator layer (IL) in turn, creating an opposite slope direction and establishing a steep band gradient across the IL, enhancing the tunneling possibility of carriers. Additionally, the band of the IGZO layer bends upward near the interface with the IL, leading to electron depletion and hole accumulation. Under illumination, a significant number of photo-excited carriers are generated. Driven by the band alignment, the photo-generated holes can tunnel through the IL from IGZO to FG and be trapped there, inducing a positive electric field that attracts electrons from the n-type IGZO layer, thereby increasing the electron density near the interface and enhancing channel conductivity. After illumination, many of the photo-excited electrons and holes recombine with each other, leading to a transient decrease in channel conductivity. However, the trapped holes in FG continue to exert a persistent positive field, maintaining the photoconductive states over time. A comparison of the band diagrams before and after light illumination is further described in Fig. S10(a) (supplementary material).

In contrast, as shown in Fig. 4(d), after applying a sufficient positive V_G pulse, the band alignment is reversed compared to the previous case, promoting the tunneling of photo-generated electrons rather than holes from IGZO to FG through IL. The trapped electrons induce a negative electric field, attracting holes in the channel and consequently decreasing the channel conductivity. This results in a negative photoresponse. The comparison of the band diagrams before and after light illumination is described in Fig. S10(b) (supplementary material). In this way, nonvolatile positive/negative photoconductive states are achieved through a ferroelectric-tunable band alignment by applying a sufficient negative/positive V_G pulse to preset the polarization before illumination.

High-performance image processing was also achieved using the MFMIS structure. Unlike conventional methods based on differential photoresponsivity ($\Delta R = R_n - R_m$), our approach leverages bidirectional photoresponse to construct optical convolution kernels, enabling precise spatial weight modulation for feature enhancement. To mitigate gradient attenuation in traditional sharpening, we implemented a programmable Laplacian kernel (k = [[0 −1 0], [−1 5 −1], [0 −1 0]]), with weights tunable in [−5, 5] via bidirectional photoresponse. This configuration amplifies central pixels (5×) while suppressing peripherals (−1×), enhancing second-order differential features. Simulations [Figs. 5(b) and 5(c)] show improved edge SNR and reduced variance, balancing feature enhancement and noise suppression in both sharpening and edge extraction.

Moreover, inspired by the antagonistic mechanisms of bipolar ON/OFF cells and temporal modulation in retinal neurons, a retinomorphic motion detection paradigm was developed.[3] As illustrated in Fig. 5(d), the system integrates a 2D retinomorphic array with a positive conductance matrix (W^1_{mn}) and a negative conductance matrix (W^2_{mn}) to perform frame difference computations. For a motion sequence spanning t_0 to tend, let X_{mn} and Y_{mn} represent normalized brightness distributions (scaled [0,1]) at t_1 and $t_1 + \Delta t$, respectively. The retinomorphic device executes the following:

$$Output = W^1 \cdot X(t_1) + W^2 \cdot Y(t_1 + \Delta t), \quad (1)$$

where · denotes the Hadamard product. Static backgrounds exhibit near-zero outputs due to conductance matrix symmetry ($\|W^1\| \approx \|W^2\|$), effectively suppressing stationary noise. Moving objects induce differential responses proportional to displacement magnitude, enabling motion detection through thresholding [Figs. 5(e)–5(f)].

In conclusion, nonvolatile bidirectional photoresponse in a fully CMOS-compatible MFMIS FeFET is achieved in this work. This originates from a ferroelectric-tunable band alignment, which enables photo-generated holes or electrons to tunnel through the IL and be trapped in the FG. Outstanding in-sensor convolutional operations, including image sharpening, edge extraction, and motion detection, have also been demonstrated based on the device. This work offers a promising route to hardware design toward high-performance sensing, computing, and memory integration systems.

See the supplementary material for details concerning the writing power consumption calculation method, GIXRD pattern of the HZO film, the locally magnified close-ups of positive and negative photoresponse, the spot size of the light source relative to the single demo device, bidirectional photoresponse of the MFMIS device under 450 nm blue light and 405 nm purple light, retention of the nonvolatile negative photoresponse after one illumination period, the bidirectional photoresponse behaviors with a lower but longer preset V_G pulse, the evidence of FE breakdown after high V_G, change in I_{ph} with progressively increased V_G in different MFMIS devices, the bidirectional photoresponse in an MIMIS FeFET, and the band diagram illustrations of nonvolatile positive and negative photoresponse mechanisms before and after light illumination.

The authors acknowledge financial support from the National Natural Science Foundation of China (Nos. 62450003, 52350195, T2222025, and 62274109).

AUTHOR DECLARATIONS

Conflict of Interest

The authors have no conflicts to disclose.

Author Contributions

Yuyan Fan and Wei Li contributed equally to this work.

Yuyan Fan: Conceptualization (equal); Data curation (equal); Formal analysis (equal); Writing – original draft (equal). **Wei Li:** Data curation (equal); Formal analysis (equal). **Jianquan Liu:** Data curation (equal). **Danyang Chen:** Data curation (equal). **Xinrui Ma:** Data curation (equal). **Tianning Cui:** Data curation (equal). **Zhiyu Lin:** Data curation (equal). **Mengwei Si:** Formal analysis (equal). **Jingquan Liu:** Funding acquisition (equal); Resources (equal). **Gang Liu:** Writing – original draft (equal); Writing – review & editing (equal). **Bobo Tian:** Funding acquisition (equal); Writing – original draft (equal); Writing – review & editing (equal). **Xiuyan Li:** Conceptualization (equal); Funding acquisition (equal); Writing – original draft (equal); Writing – review & editing (equal).

DATA AVAILABILITY

The data that support the findings of this study are available from the corresponding authors upon reasonable request.

REFERENCES

[1]F. Zhou and Y. Chai, "Near-sensor and in-sensor computing," Nat. Electron. **3**(11), 664–671 (2020).
[2]L. Mennel, J. Symonowicz, S. Wachter, D. K. Polyushkin, A. J. Molina-Mendoza, and T. Mueller, "Ultrafast machine vision with 2D material neural network image sensors," Nature **579**(7797), 62–66 (2020).
[3]Z. Zhang, S. Wang, C. Liu, R. Xie, W. Hu, and P. Zhou, "All-in-one two-dimensional retinomorphic hardware device for motion detection and recognition," Nat. Nanotechnol. **17**(1), 27–32 (2022).
[4]C. Wan, P. Cai, M. Wang, Y. Qian, W. Huang, and X. Chen, "Artificial sensory memory," Adv. Mater. **32**(15), 1902434 (2020).
[5]Y. Chai, "In-sensor computing for machine vision," Nature **579**(7797), 32–33 (2020).
[6]L. Wang, H. Wang, J. Liu, Y. Wang, H. Shao, W. Li, M. Yi, H. Ling, L. Xie, and W. Huang, "Negative photoconductivity transistors for visuomorphic computing," Adv. Mater. **36**(38), 2403538 (2024).
[7]T. Wan, B. Shao, S. Ma, Y. Zhou, Q. Li, and Y. Chai, "In-sensor computing: materials, devices, and integration technologies," Adv. Mater. **35**(37), 2203830 (2023).
[8]M. A. Zidan, J. P. Strachan, and W. D. Lu, "The future of electronics based on memristive systems," Nat. Electron. **1**(1), 22–29 (2018).
[9]T. Tuma, A. Pantazi, M. Le Gallo, A. Sebastian, and E. Eleftheriou, "Stochastic phase-change neurons," Nat. Nanotechnol. **11**(8), 693–699 (2016).
[10]T. Ohno, T. Hasegawa, T. Tsuruoka, K. Terabe, J. K. Gimzewski, and M. Aono, "Short-term plasticity and long-term potentiation mimicked in single inorganic synapses," Nat. Mater. **10**(8), 591–595 (2011).
[11]F. Liao, Z. Zhou, B. J. Kim, J. Chen, J. Wang, T. Wan, Y. Zhou, A. T. Hoang, C. Wang, J. Kang, J.-H. Ahn, and Y. Chai, "Bioinspired in-sensor visual adaptation for accurate perception," Nat. Electron. **5**(2), 84–91 (2022).
[12]T. Jiang, Y. Wang, Y. Zheng, L. Wang, X. He, L. Li, Y. Deng, H. Dong, H. Tian, Y. Geng, L. Xie, Y. Lei, H. Ling, D. Ji, and W. Hu, "Tetrachromatic vision-inspired neuromorphic sensors with ultraweak ultraviolet detection," Nat. Commun. **14**(1), 2281 (2023).
[13]Y. Zhang, L. Wang, Y. Lei, B. Wang, Y. Lu, Y. Yao, N. Zhang, D. Lin, Z. Jiang, H. Guo, J. Zhang, and H. Hu, "Self-powered bidirectional photoresponse in high-detectivity WSe_2 phototransistor with asymmetrical van der Waals stacking for retinal neurons emulation," ACS Nano **16**(12), 20937–20945 (2022).

[14]M. Wang, X. Zhuang, F. Liu, Y. Chen, Z. Sa, Y. Yin, Z. Lv, H. Wei, K. Song, B. Cao, and Z-x Yang, "New approach to low-power-consumption, high-performance photodetectors enabled by nanowire source-gated transistors," Nano Lett. **22**(23), 9707–9713 (2022).
[15]M. Wang, F. Liu, T. Zhang, G. Wang, Z. Sa, Z. Zang, D. Qi, K. Song, P. Cui, and Z.-x. Yang, "Toward low-power-consumption source-gated phototransistor," Appl. Phys. Lett. **124**(20), 203504 (2024).
[16]J. Liu, W. Han, E. Hong, M. Deng, Z. Li, L. Wu, and X. Fang, "In-memory sensing and logic processing in negative capacitance phototransistors," Adv. Funct. Mater. **35**, 2425350 (2025).
[17]Q. Yang, Z. Luo, D. Zhang, M. Zhang, X. Gan, J. Seidel, Y. Liu, Y. Hao, and G. Han, "Controlled optoelectronic response in van der Waals heterostructures for in-sensor computing," Adv. Funct. Mater. **32**(45), 2207290 (2022).
[18]Y. Lee, J. Kwon, E. Hwang, C.-H. Ra, W. J. Yoo, J.-H. Ahn, J. H. Park, and J. H. Cho, "High-performance perovskite–graphene hybrid photodetector," Adv. Mater. **27**(1), 41–46 (2015).
[19]F. Li, C. Ma, H. Wang, W. Hu, W. Yu, A. D. Sheikh, and T. Wu, "Ambipolar solution-processed hybrid perovskite phototransistors," Nat. Commun. **6**, 8238 (2015).
[20]S. C. Singh, Y. Peng, J. Rutledge, and C. Guo, "Photothermal and joule-heating-induced negative-photoconductivity-based ultraresponsive and near-zero-biased copper selenide photodetectors," ACS Appl. Electron. Mater. **1**(7), 1169–1178 (2019).
[21]A. Grillo, E. Faella, A. Pelella, F. Giubileo, L. Ansari, F. Gity, P. K. Hurley, N. McEvoy, and A. Di Bartolomeo, "Coexistence of negative and positive photoconductivity in few-layer $PtSe_2$ field-effect transistors," Adv. Funct. Mater. **31**(43), 2105722 (2021).
[22]R. Wang, J. L. Wang, T. Liu, Z. He, H. Wang, J. W. Liu, and S. H. Yu, "Controllable inverse photoconductance in semiconducting nanowire films," Adv. Mater. **34**(36), 2204698 (2022).
[23]L. Pi, P. Wang, S.-J. Liang, P. Luo, H. Wang, D. Li, Z. Li, P. Chen, X. Zhou, F. Miao, and T. Zhai, "Broadband convolutional processing using band-alignment-tunable heterostructures," Nat. Electron. **5**(4), 248–254 (2022).
[24]A. Cao, S. Li, H. Chen, M. Deng, X. Xu, L. Shang, Y. Li, A. Cui, and Z. Hu, "A polar-switchable and controllable negative phototransistor for information encryption," Mater. Horiz. **10**(11), 5099–5109 (2023).
[25]F. Li, J. Zeng, Y. Zhao, L. Zhu, Y. Zhou, Z. Wang, Z. Wang, Y. Zhang, G. Liu, J. Xiong, W. Gao, M. Yang, J. Li, N. Huo, and Y. Sun, "High hole mobility van der Waals junction field-effect transistors based on Te/GaAs for multimode photodetection and logic applications," ACS Appl. Mater. Interfaces **17**(12), 18655–18665 (2025).
[26]J. You, Z. Han, N. Zhang, Q. Zhang, Y. Zhang, Y. Liu, Y. Li, J. Ao, Z. Jiang, Z. Zhong, H. Guo, H. Hu, L. Wang, and Z. Zhu, "All-optic logical operations based on the visible-near infrared bipolar optical response," Adv. Sci. **11**(40), 2404336 (2024).
[27]X. Shi, Y. Xu, W. Liu, C. Jin, S. Wang, J. Sun, and J. Yang, "Organic heterojunction phototransistors with bi-directional photoresponse for vision biomimetics," Adv. Funct. Mater. **34**(32), 2401534 (2024).
[28]L. Xie, X. Chen, Z. Dong, Q. Yu, X. Zhao, G. Yuan, Z. Zeng, Y. Wang, and K. Zhang, "Nonvolatile photoelectric memory induced by interfacial charge at a ferroelectric PZT-gated black phosphorus transistor," Adv. Elect. Mater. **5**(8), 1900458 (2019).
[29]X. Lei, J. Liu, S. Liu, L. Zhang, M. He, and R. Huang, "Ultrasensitive retinomorphic dim-light vision with in-sensor convolutional processing based on reconfigurable perovskite-Bi_2O_2Se heterotransistors," in *International Electron Devices Meeting (IEDM)* (IEEE, 2023), pp. 1–4.
[30]D. Xue, W. Gong, C. Yan, Y. Zhang, J. Lu, Y. Yin, J. Zhang, Z. Wang, L. Huang, and L. Chi, "Boosting bidirectional photoresponse with wavelength selectivity through ambipolar transport modulation," Adv. Funct. Mater. **34**(38), 2402884 (2024).
[31]Q. Dai, M. Pei, J. Guo, Q. Wang, Z. Hao, H. Wang, Y. Li, L. Li, K. Lu, Y. Yan, Y. Shi, and Y. Li, "Integration of image preprocessing and recognition functions in an optoelectronic coupling organic ferroelectric retinomorphic neuristor," Mater. Horiz. **10**(8), 3061–3071 (2023).
[32]T. Ahmed, S. Kuriakose, S. Abbas, M. J. S. Spencer, M. A. Rahman, M. Tahir, Y. Lu, P. Sonar, V. Bansal, M. Bhaskaran, S. Sriram, and S. Walia, "Multifunctional optoelectronics via harnessing defects in layered black phosphorus," Adv. Funct. Mater. **29**(39), 1901991 (2019).
[33]J. Han, J. Wang, M. Yang, X. Kong, X. Chen, Z. Huang, H. Guo, J. Gou, S. Tao, Z. Liu, Z. Wu, Y. Jiang, and X. Wang, "Graphene/organic semiconductor heterojunction phototransistors with broadband and bi-directional photoresponse," Adv. Mater. **30**(49), 1804020 (2018).
[34]Y. Wang, E. Liu, A. Gao, T. Cao, M. Long, C. Pan, L. Zhang, J. Zeng, C. Wang, W. Hu, S.-J. Liang, and F. Miao, "Negative photoconductance in van der Waals heterostructure-based floating gate phototransistor," ACS Nano **12**(9), 9513–9520 (2018).
[35]Y.-X. Hou, Y. Li, Z.-C. Zhang, J.-Q. Li, D.-H. Qi, X.-D. Chen, J.-J. Wang, B.-W. Yao, M.-X. Yu, T.-B. Lu, and J. Zhang, "Large-scale and flexible optical synapses for neuromorphic computing and integrated visible information sensing memory processing," ACS Nano **15**(1), 1497–1508 (2021).
[36]H. Zhang, H. Li, F. Wang, X. Song, Z. Xu, D. Wei, J. Zhang, Z. Dai, Y. Ren, Y. Ye, X. Ren, and J. Yao, "$PtSe_2$ field-effect phototransistor with positive and negative photoconductivity," ACS Appl. Electron. Mater. **4**(11), 5177–5183 (2022).
[37]J. Chen, P. Suo, W. Zhang, H. Ma, J. Fu, D. Li, X. Lin, X. Yan, W. Liu, Z. Jin, G.-H. Ma, and J. Yao, "Photocarrier-driven emergence of negative photoconductivity in semimetal $MoTe_2$ films revealed with terahertz spectroscopy," J. Phys. Chem. C **126**(22), 9407–9415 (2022).
[38]Q. Wang, F. Yang, Y. Zhang, M. Chen, X. Zhang, S. Lei, R. Li, and W. Hu, "Space-confined strategy toward large-area two-dimensional single crystals of molecular materials," J. Am. Chem. Soc. **140**(16), 5339–5342 (2018).
[39]C. Xu, P. He, J. Liu, A. Cui, H. Dong, Y. Zhen, W. Chen, and W. Hu, "A general method for growing two-dimensional crystals of organic semiconductors by 'solution epitaxy,'" Angew. Chem., Int. Ed. **55**(33), 9519–9523 (2016).
[40]Y. Yuan, Q. Yao, J. Zhang, K. Wang, W. Zhang, T. Zhou, H. Sun, and J. Ding, "Negative photoconductivity in Cs_4PbBr_6 single crystal," Phys. Chem. Chem. Phys. **22**(25), 14276–14283 (2020).
[41]S. Paramanik and A. J. Pal, "Combining negative photoconductivity and resistive switching towards in-memory logic operations," Nanoscale **15**(10), 5001–5010 (2023).
[42]M. A. Haque, J.-L. Li, A. L. Abdelhady, M. I. Saidaminov, D. Baran, O. M. Bakr, S.-H. Wei, and T. Wu, "Transition from positive to negative photoconductance in doped hybrid perovskite semiconductors," Adv. Opt. Mater. **7**(22), 1900865 (2019).
[43]M. Si, Z. Lin, Z. Chen, X. Sun, H. Wang, and P. D. Ye, "Scaled indium oxide transistors fabricated using atomic layer deposition," Nat. Electron. **5**(3), 164–170 (2022).
[44]M. Si, A. Charnas, Z. Lin, and P. D. Ye, "Enhancement-mode atomic-layer-deposited In_2O_3 transistors with maximum drain current of 2.2 A/mm at drain voltage of 0.7 V by low-temperature annealing and stability in hydrogen environment," IEEE Trans. Electron Devices **68**(3), 1075–1080 (2021).
[45]D. Li, H. Ren, Y. Chen, Y. Tang, K. Liang, Y. Wang, F. Li, G. Liu, L. Meng, and B. Zhu, "Bidirectionally photoresponsive optoelectronic transistors with dual photogates for all-optical-configured neuromorphic vision," Adv. Funct. Mater. **33**(42), 2303198 (2023).
[46]D. Li, Y. Chen, H. Ren, Y. Tang, S. Zhang, Y. Wang, L. Xing, Q. Huang, L. Meng, and B. Zhu, "An active-matrix synaptic phototransistor array for in-sensor spectral processing," Adv. Sci. **11**(39), 2406401 (2024).
[47]S. Zhang, P. Xiao, X. Hong, R. Hong, C. Liu, Q. Tian, W. Su, C. Ma, X. Liu, K. Li, J. C. Ho, Y. Lv, Q. Hong, L. Liao, and X. Zou, "All-in-one hardware devices with event-based vision sensor arrays for image sensing, computing, and learning," Adv. Funct. Mater. **33**(44), 2306173 (2023).
[48]Z. Zheng, L. Jiao, D. Zhang, C. Sun, Z. Zhou, X. Wang, G. Liu, Q. Kong, Y. Chen, K. Ni, and X. Gong, "BEOL-compatible MFMIS ferroelectric/anti-ferroelectric FETs—Part I: Experimental results with boosted memory window," IEEE Trans. Electron Devices **71**(3), 1827–1833 (2024).
[49]Z. Zheng, D. Zhang, L. Jiao, C. Sun, Z. Zhou, Y. Chen, Q. Kong, X. Wang, G. Liu, K. Ni, and X. Gong, "BEOL-compatible MFMIS ferroelectric/anti-ferroelectric FETs—Part II: Mechanism with load line analysis and scaling strategy," IEEE Trans. Electron Devices **71**(9), 5325–5331 (2024).
[50]Z. Zheng, C. Sun, L. Jiao, D. Zhang, Z. Zhou, in X. Wang, G. Liu, Q. Kong, Y. Chen, K. Ni, and X. Gong, "Boosting the memory window of the BEOL-compatible MFMIS ferroelectric/ anti-ferroelectric FETs by charge injection,"

in *IEEE Symposium on VLSI Technology and Circuits (VLSI Technology and Circuits)* (IEEE, 2022), pp. 389–390.
[51]Z. Zheng, L. Jiao, Z. Zhou, Y. Wang, L. Liu, in K. Han, C. Sun, Q. Kong, D. Zhang, X. Wang, K. Ni, and X. Gong, "First demonstration of work function-engineered BEOL-compatible IGZO non-volatile MFMIS AFeFETs and their co-integration with volatile-AFeFETs," in *IEEE Symposium on VLSI Technology and Circuits (VLSI Technology and Circuits)* (IEEE, 2023), pp. 1–2.
[52]Y. Sun, Y. Wang, Z. Wang, L. Jiang, Z. Hou, L. Dai, J. Zhao, Y. H. Xie, L. Zhao, Z. Jiang, W. Ren, and G. Niu, "Ambipolar MoS_2 field effect transistors with negative photoconductivity and high responsivity using an ultrathin epitaxial ferroelectric gate," Adv. Funct. Mater. **34**(37), 2402185 (2024).
[53]A. Kumar, K. Intonti, L. Viscardi, O. Durante, A. Pelella, O. Kharsah, S. Sleziona, F. Giubileo, N. Martucciello, P. Ciambelli, M. Schleberger, and A. Di Bartolomeo, "Memory effect and coexistence of negative and positive photoconductivity in black phosphorus field effect transistor for neuromorphic vision sensors," Mater. Horiz. **11**(10), 2397–2405 (2024).
[54]C. Jin, J. Wang, S. Yang, Y. Ding, J. Chang, W. Liu, Y. Xu, X. Shi, P. Xie, J. C. Ho, C. Wan, Z. Zheng, J. Sun, L. Liao, and J. Yang, "Bidirectional photovoltage-driven oxide transistors for neuromorphic visual sensors," Adv. Mater. **37**(1), 2410398 (2025).